



Two-photon cross-section calculations for krypton in the 190–220 nm range

DAVID SHEKHTMAN,^{1,*}  MUHAMMAD AMMAR MUSTAFA,¹  AND NICHOLAUS JOSEPH PARZIALE^{1,2} 

¹Stevens Institute of Technology, 1 Castle Point, Hoboken, New Jersey 07030, USA

²e-mail: nick.parziale@gmail.com

*Corresponding author: davshe98@gmail.com

Received 23 September 2020; revised 27 October 2020; accepted 27 October 2020; posted 29 October 2020 (Doc. ID 410806); published 30 November 2020

This paper presents multi-path, two-photon excitation cross-section calculations for krypton, using first-order perturbation theory. For evaluation of the two-photon-transition matrix element, this paper formulates the two-photon cross-section calculation as a matrix mechanics problem. From a finite basis of states, consisting of $4p$, $5s$, $6s$, $7s$, $5p$, $6p$, $4d$, $5d$, and $6d$ orbitals, electric dipole matrix elements are constructed, and a Green's function is expressed as a truncated, spectral expansion of solutions, satisfying the Schrödinger equation. Electric dipole matrix elements are evaluated via tabulated oscillator strengths, and where those are unavailable, quantum-defect theory is used. The relative magnitudes of two-photon cross-sections for eight krypton lines in the 190–220 nm range are compared to experimental excitation spectra with good agreement. This work provides fundamental physical understanding of the Kr atom, which adds to experimental observations of relative fluorescence intensity. This is valuable when comparing excitation schemes in different environments for krypton fluorescence experiments. We conclude that two-photon excitation at 212.556 nm is optimal for single-laser, krypton tagging velocimetry or krypton planar laser-induced fluorescence. © 2020 Optical Society of America

<https://doi.org/10.1364/AO.410806>

1. INTRODUCTION

There are multiple excitation lines for the two-photon excitation of Kr in the 190–220 nm range: 192.749 nm, 193.494 nm, 193.947 nm, 202.316 nm, 204.196 nm, 212.556 nm, 214.769 nm, and 216.667 nm. The optimal choice of excitation line for krypton fluorescence experiments is subject to test requirements, such as signal-to-noise ratio (SNR), background luminosity, and, in the case of krypton tagging velocimetry (KTV), the write/read delay time. When determining the optimal scheme for krypton fluorescence experiments, evaluating the two-photon cross-section is the starting point and, as such, the motivation for the current work.

Methods for calculating two-photon cross-sections include first-order perturbation theory, the Green's function method, R-matrix theory, and time-dependent density-functional theory (TDDFT). First-order perturbation theory for multiphoton excitation and ionization is described by Lambropoulos [1] who provides a thorough review of multiphoton processes and calculations, and demonstrates the matrix mechanics nature of the problem. Khambatta *et al.* [2,3] uses the first-order perturbation theory of Lambropoulos [1] and the oscillator formulas from Hillborn [4] to calculate two- and three-photon

cross-sections for argon and krypton. He presents both a single-path and multi-path calculation. However, that calculation is limited by the availability of tabulated Einstein coefficients. Additionally in that work, the dipole matrix element is asymmetric, thus unable to capture the mathematical symmetry of the two-photon transition matrix element. A similar single-path calculation for the excitation of Kr to the $6p$ level was made by Bokor *et al.* [5]. The calculations in Bokor *et al.* [5] and Khambatta *et al.* [2,3] serve as important benchmarks for two-photon cross-section calculation and $(2 + 1)$ photoionization modeling. Mustafa *et al.* [6] used the single-path approximation to estimate the two-photon cross-section for the 212.556 nm excitation line for krypton. An additional motivation for the current work was to assess the validity of the results of Mustafa *et al.* [6] and explore whether other excitation lines might result in higher fluorescence.

In the first-order perturbation formulation of multiphoton excitation, infinite excitation pathways exist, and summation occurs over an infinite space of virtual states, both bound and unbound. If one does not assume a functional form for a finite (truncated) basis of virtual states, the calculation of the multiphoton transition matrix element can be difficult. Numerous researchers developed alternative techniques to avoid explicitly

summing over a finite basis of states using an analytical Green's function. By making a central-field approximation, and by applying quantum-defect theory (QDT), a phenomenological Green's function was derived, as done in both Lambropoulos [1] and McGuire [7,8]. The main problem with this Green's function approach is the lack of spectral resolution; that is, the phenomenological Green's function for two-photon excitation is unable to resolve fine-structure effects, which are necessary to calculate closely clustered excitation spectra. Despite this, it provides good estimates of the magnitude of the two-photon cross-section.

TDDFT is a modern computational approach to modeling time-dependent quantum systems [9]. It can be used to generate excitation spectra for atoms and molecules. However, for a large atom such as krypton with many electrons, an accurate, initial guess for charge distribution and wave functions would need to be made, especially to observe fine-structure effects. R-matrix theory represents another approach to multiphoton excitation [10]. It directly solves the Schrödinger equation. However, it is more computationally difficult to implement for a large multi-electron atom such as Kr, and currently, only a formulation for multiphoton ionization is readily available.

As stated, the motivation for this work is krypton fluorescence experiments, which have attracted great interest over the last decade because of their promise in making fundamental contributions in subsonic and supersonic combustion in addition to supersonic and hypersonic aerodynamics [11]. Two such experiments are krypton planar laser-induced fluorescence (Kr-PLIF) and KTV. Kr-PLIF and KTV are performed by the addition of a small mole fraction of Kr to a high-speed/reacting flow. This strategy has enabled the non-intrusive measurement of important quantities such as density, temperature, mixing fraction, and velocity that were not previously possible in difficult-to-measure gas flows.

Initial Kr-PLIF work was performed at 214.7 nm [12–16], which now includes thermometry [17–19]. Additionally, the 204.196 nm line has also been used for Kr-PLIF [20–22]. Experimental Kr-PLIF excitation line comparisons have been performed by [23,24], with the observation that the 212.556 nm line was superior. High-speed Kr-PLIF was performed at 212.556 nm by Grib *et al.* [25]. Original KTV work relied on write-line excitation at 214.769 nm to generate the metastable Kr state [26–31]. In more recent KTV work [6,32] and in this paper, we observe higher SNR for single-laser, unfiltered KTV with a 212.556 nm write-line excitation; additionally, we observe that two-photon excitation at 216.667 nm is optimal for two-laser KTV where there is a need for spatial filtering to eliminate background luminosity.

In this paper, we calculate the two-photon cross-sections of Kr to (1) remove any ambiguity in the superiority of the 212.556 nm line for Kr-PLIF and single-laser KTV; (2) provide fundamental physical insights to verify the Richardson *et al.* [23] excitation spectrum; (3) provide reliable cross-sections for modeling other Kr excitation schemes; and (4) prepare a framework for calculating multiphoton excitation spectra for other noble gas atoms. Herein, we detail our calculation method and compare the results of those calculations to experimental results with success.

2. RELATION OF CROSS-SECTION TO SIGNAL-TO-NOISE RATIO

By definition, the fluorescence signal, Q , from an atomic transition is calculated per Eckbreth [33] as

$$Q = hf_e N_u A \Omega V / (4\pi), \quad (1)$$

where h is Planck's constant, f_e is the frequency of emitted light, N_u is the population of the upper level, A is the overall Einstein coefficient, Ω is the collection solid angle, and V is the emitting volume. As Eq. (1) shows, $\text{SNR} \propto Q \propto N_u$.

During a laser pulse, the two-photon excited state population, denoted by N_f , is governed by

$$\frac{dN_f}{dt} = W_{f,g} N_g - (W_{pi} + A_f + W_{f,g} + q) N_f, \quad (2)$$

where $W_{f,g}$ is the two-photon excitation rate from the ground state $|g\rangle$ to the final state, W_{pi} is one-photon photoionization rate from final state $|f\rangle$ to the ionized state, N_g is the population of the ground state Kr atoms, A_f is the overall Einstein coefficient, and q is the quenching rate for the excited state. At the rising edge of the laser pulse, N_f is small and is approximately proportional to $W_{f,g}$:

$$N_f \approx W_{f,g} N_g \Delta t. \quad (3)$$

The one-photon photoionization rate W_{pi} in Eq. (2) is

$$W_{pi} = F \sigma_{pi}, \quad (4)$$

where the photoionization cross-section σ_{pi} is calculated by Khambatta *et al* [2] as

$$\sigma_{pi} = \frac{8 \times 10^{-18}}{Z_e \sqrt{\frac{-E_f}{Ry} \left(\frac{\hbar\omega_L}{-E_f} \right)^3}}. \quad (5)$$

In Eq. (5), $Z_e = 1$ is the charge of the Kr ion, Ry is the Rydberg constant, and E_f is the energy of the final state. The one-photon photoionization cross-section σ_{pi} is approximately the same for the different Kr excitation lines because of the closely clustered energies of the eight states. Therefore, the two-photon cross-section $\sigma_o^{(2)}$ is the most significant in determining the excitation spectrum for the Kr lines. Researchers, such as Saito *et al.* [34] and Khambatta *et al.* [2], respectively, developed detailed analytical and numerical population models, featuring Eq. (2). In this work, the solution to Eq. (2) is not explored beyond Eq. (3).

$W_{f,g}$ is defined as

$$W_{f,g} = F^2 \sigma^{(2)}, \quad (6)$$

where $\sigma^{(2)}$ is the two-photon excitation rate coefficient, and $F = I/(\hbar\omega_L)$ is the photon flux. I is the laser intensity; \hbar is the reduced Planck's constant; and ω_L is the laser angular frequency. The rate coefficient, $\sigma^{(2)}$, is a function of the excitation wavelength and is directly proportional to the cross-section $\sigma_o^{(2)}$. Consequently, the wavelength with the highest value of $\sigma_o^{(2)}$ will result in the highest fluorescence signal after the laser pulse. That is, $\text{SNR} \propto \sigma_o^{(2)}$ right after the rising edge of the laser pulse.

3. TWO-PHOTON CROSS-SECTION CALCULATION FOR KRYPTON IN THE 190–220 NM EXCITATION RANGE

A two-photon cross-section calculation was conducted using multi-path, first-order accurate perturbation theory. A Hartree–Fock radial wave function of the krypton ground state ($4p^6\ ^1S_0$) was assumed [35], and oscillator strength (OS) formulas were used upon the availability of NIST transition probabilities and data [36] (Russell–Saunders Notation $^{2S+1}L_J$ with, $S = 0$, $L = 0$ and $J = 0$). We note that a Kr gas mixture with naturally occurring isotope mole fractions was considered because the NIST line spectra database presents spectroscopic data for a naturally occurring mixture of Kr [36], and the laser pulse width is at least two orders of magnitude greater than the isotopic shifts of Kr. Additionally, QDT was used to calculate electric dipole matrix elements when NIST transition probabilities were unlisted. This last inclusion of QDT is key to the success of our approach, as it enabled the inclusion of additional excitation pathways not included in previous works; and it determined the sign of all pathway contributions to the two-photon matrix element.

When QDT is used to evaluate the purely radial matrix elements, $\langle r \rangle$ scaled hydrogen radial wave functions are constructed to represent excited Kr states. This is because a Hartree–Fock calculation showed that excited krypton states exhibited hydrogenic behavior and could be approximated well by quantum-defect radial wave functions that are calibrated by NIST line data.

The two-photon cross-section $\sigma_o^{(2)}$ is independent of laser intensity, time, and Kr concentration. It is a constant, and it is a solution to the time-independent, non-relativistic Schrödinger equation (relativistic effects were neglected in the Schrödinger equation because the energy of the laser was much less than the rest energy of an electron $3\hbar\omega_L \ll m_e c^2$ [37]). At the rising edge of the laser pulse, $\sigma_o^{(2)} \propto \sigma^{(2)} \propto Q \propto \text{SNR}$ [33]. The two-photon cross-section $\sigma_o^{(2)}$ is related to the two-photon excitation rate-coefficient $\sigma^{(2)}$ via the lineshape function $g(2\omega_L)$ as

$$\sigma^{(2)} = \sigma_o^{(2)} g(2\omega_L). \quad (7)$$

The two-photon excitation cross-section is calculated as

$$\sigma_o^{(2)} = (2\pi)^3 (\alpha)^2 \omega_L^2 |M_{fg}^{(2)}|^2 a_o^4, \quad (8)$$

where α is the fine structure constant, a_o is the Bohr radius, and $M_{fg}^{(2)}$ is the two-photon-transition matrix element. The line shape function $g(2\omega_L)$ is assumed to be of Gaussian form with a peak:

$$g(2\omega_L = \omega_T) = \frac{2\sqrt{\ln(2)}/\pi}{\sqrt{2(\Delta\omega_L)^2 + (\Delta\omega_T)^2}}. \quad (9)$$

The linewidth of the laser is $\Delta\omega_L$ (1350 MHz in this work), and the Doppler linewidth, $\Delta\omega_T$, is calculated by

$$\Delta\omega_T = (2\omega_L) \sqrt{\frac{8\ln(2)k_b T}{m_{kr} c^2}}, \quad (10)$$

where k_b is the Boltzmann constant, c is the speed of light, m_{kr} is the mass of one krypton atom, and T is the temperature of the Kr gas mixture.

The two-photon-transition matrix element is expressed as

$$M_{fg}^{(2)} = \sum_{k=g}^{\infty} \frac{\langle f | \hat{\epsilon} \cdot \vec{r} | k \rangle \langle k | \hat{\epsilon} \cdot \vec{r} | g \rangle}{\omega_k - \omega_g - \omega_L}. \quad (11)$$

For practical calculation on a computer, the summation over the intermediate state index k is truncated at the N th state. Therefore, the transition matrix element,

$$M_{fg}^{(2)} = \sum_{k=g}^N \frac{\langle f | \hat{\epsilon} \cdot \vec{r} | k \rangle \langle k | \hat{\epsilon} \cdot \vec{r} | g \rangle}{\omega_k - \omega_g - \omega_L}, \quad (12)$$

is summed over a finite basis of states, such as those listed in Table 3. The truncation criterion for two-photon excitation is determined by a constraint on the maximum principal quantum number n of a bound state: n_{\max} . As n becomes large, the expected radius of a one-electron atom of effective nuclear charge Z_e is $\langle r \rangle = n^2/Z_e$ in Bohr radii [38]. Per Park [39], the $\langle r \rangle$ is proportional to the Debye length d_D :

$$n_{\max} = \sqrt{\frac{Z_e d_D}{10a_o}} \approx \left(\frac{Z_e^2 \epsilon_o k_b}{e^2 \left(\frac{N_e}{T_e} + \frac{N_i}{T_i} \right) (10a_o)^2} \right)^{\frac{1}{4}}, \quad (13)$$

where N_e/V is the electron number density, N_i/V is the ion number density, T_e is the electron temperature, and T_i is the Kr ion temperature. The factor of $10a_o$ describes approximately the krypton van der Waals diameter and represents a 90% reduction in the Debye potential, Φ_D , which is non-dimensionally described by $\Phi_D = 1/r \exp(-ra_o/d_D)$. For the $(2+1)$ resonance-enhanced multiphoton excitation (REMPI) of Kr at laser wavelength $\lambda_L = 212.556$ nm, room temperature $T = 298$ K, and pressure $P = 1$ torr, the electron temperature is $T_e = 27626$ K, and number densities are calculated as $N_e/V = N_i/V = 1.62 \times 10^{21}$ electrons/m³. The electron temperature was obtained from $2(3\hbar\omega_L - |E_{\text{ion}}|)/3(k_b)$ [40], and number densities were obtained via the analytical population model of Saito *et al.* [34]. Assuming $Z_e = 1$ for the Kr ion, the result is $n_{\max} = 7.42$. Therefore, N accommodates all states with a principal quantum number equal to or less than 7: $n \leq 7$. This is convenient because NIST transition probability data are limited for states with $n \leq 8$ [36].

An approximate Green's function, expressed as a truncated spectral expansion, is nested in the center of the expression for $M_{fg}^{(2)}$:

$$G(\vec{r}, \vec{r}') = \sum_{k=g}^N \frac{|k\rangle \langle k|}{\omega_k - \omega_g - \omega_L}. \quad (14)$$

Since Green's functions are symmetric about variable exchange ($\vec{r} \leftrightarrow \vec{r}'$), $G(\vec{r}, \vec{r}') = G(\vec{r}', \vec{r})$, so $M_{fg}^{(2)} = M_{gf}^{(2)}$. This mathematical property is a fundamental deviation from the OS approach in Khambatta *et al.* [2], which is one-sided and asymmetric. Therefore, the use of oscillator formulas, while valid, causes the loss of symmetry in the transition matrix element.

This symmetry loss is problematic in describing higher-order multiphoton excitation (three-photon and higher).

$M_{fg}^{(2)}$ is a double tensor contraction of an infinite matrix space, $M = DGD$. More importantly, due to the invariance of multiphoton excitation with respect to the reference frame and basis $|k\rangle$, $M = DGD$ is a symmetric, rank-2 tensor.

The evaluation of $M_{fg}^{(2)}$ requires the evaluation of two reduced matrix elements of the form

$$\langle i | \hat{\epsilon} \cdot \vec{r} | j \rangle = D_{ij}, \quad (15)$$

where D_{ij} is an element of the matrix representation of the dipole operator D :

$$D = \begin{bmatrix} \langle g | \hat{\epsilon} \cdot \vec{r} | g \rangle & \langle g | \hat{\epsilon} \cdot \vec{r} | 1 \rangle & \cdots & \langle g | \hat{\epsilon} \cdot \vec{r} | N \rangle \\ \langle 1 | \hat{\epsilon} \cdot \vec{r} | g \rangle & \langle 1 | \hat{\epsilon} \cdot \vec{r} | 1 \rangle & \cdots & \langle 1 | \hat{\epsilon} \cdot \vec{r} | N \rangle \\ \langle 2 | \hat{\epsilon} \cdot \vec{r} | g \rangle & \langle 2 | \hat{\epsilon} \cdot \vec{r} | 1 \rangle & \cdots & \langle 2 | \hat{\epsilon} \cdot \vec{r} | N \rangle \\ \vdots & \vdots & \ddots & \vdots \\ \langle N | \hat{\epsilon} \cdot \vec{r} | g \rangle & \langle N | \hat{\epsilon} \cdot \vec{r} | 1 \rangle & \cdots & \langle N | \hat{\epsilon} \cdot \vec{r} | N \rangle \end{bmatrix}. \quad (16)$$

The two indices i, j of the matrix D represent the final state $|i\rangle$ and initial state $|j\rangle$, respectively. The dipole operator, $\hat{\epsilon} \cdot \vec{r}$, describes the rotation of two electric charges of opposite sign by an external electric field. The denominator of Eq. (12),

$$G_{ii} = \frac{1}{\omega_i - \omega_g - \omega_L}, \quad (17)$$

can also be rewritten in matrix form as a diagonal matrix G :

$$G = \begin{bmatrix} \frac{1}{\omega_g - \omega_g - \omega_L} & 0 & \cdots & 0 \\ 0 & \frac{1}{\omega_1 - \omega_g - \omega_L} & \ddots & \vdots \\ \vdots & \ddots & \ddots & \vdots \\ 0 & 0 & \cdots & \frac{1}{\omega_N - \omega_g - \omega_L} \end{bmatrix}. \quad (18)$$

G is the matrix representation of the Green's function, Eq. (14). Rewriting Eq. (12), the transition matrix element can be represented in matrix form:

$$M_{fg}^{(2)} = \sum_{k=g}^N D_{fk} G_{kk} D_{kg} = \hat{\epsilon}_f^T D G D \hat{\epsilon}_g, \quad (19)$$

where $\hat{\epsilon}_i$ is a unit vector that identifies the state of the system. For example, the vector representations of states $|g\rangle$, $|1\rangle$, $|2\rangle$, and $|N\rangle$ are

$$\hat{\epsilon}_g = \begin{bmatrix} 1 \\ 0 \\ 0 \\ \vdots \\ 0 \end{bmatrix}, \quad \hat{\epsilon}_1 = \begin{bmatrix} 0 \\ 1 \\ 0 \\ \vdots \\ 0 \end{bmatrix}, \quad \hat{\epsilon}_2 = \begin{bmatrix} 0 \\ 0 \\ 1 \\ \vdots \\ 0 \end{bmatrix}, \quad \text{and} \quad \hat{\epsilon}_N = \begin{bmatrix} 0 \\ 0 \\ 0 \\ \vdots \\ 1 \end{bmatrix}. \quad (20)$$

Equation (19) substantiates to a rank-2 tensor contraction of the Green's function matrix G . The f^{th} row of matrix D is post-multiplied by the matrix G , which is then post-multiplied by the g^{th} column of matrix D , resulting in the scalar $M_{fg}^{(2)}$.

A. Calculation of Dipole Matrix Elements D_{ij} Using QDT

In this section, the dipole matrix elements D_{ij} are calculated via the central-field approximation [38,41], which allows one to separate the effects of angular and radial components in the Schrödinger equation, expressed in spherical coordinates. This allows a state $|k\rangle$ to be expressed as a product of one-electron, radial wave functions $R_{nl}(r) \cdot \prod_p R_p(r_p)$ multiplied by a tensor spherical harmonic $\mathbf{Y}_{JM}^{LS}(\theta, \phi)$. Here, subscript p denotes an unexcited krypton electron, and nl denotes the quantum numbers of the valence electron to be excited by the laser. This state is represented as $|\mathbf{n}LSJM\rangle$, assuming LS spin-orbit coupling. The radius of the excited valence electron from the Kr nucleus is r . The orientation of its angular momentum is described by azimuth angle θ and polar angle ϕ . The set of all principal quantum numbers for the Kr atom is \mathbf{n} , and the principal quantum number of the excited electron is n . L is the total orbital angular momentum quantum number of the atom, and l is the single-electron angular momentum number of the excited electron. S is the total electron spin quantum number of the atom. For a true dipole moment transition, S remains constant because the dipole moment operator $\hat{\epsilon} \cdot \vec{r}$ does not act on electron spin coordinates. The dipole moment operator is written solely in terms of scalar spherical harmonics [41]:

$$\hat{\epsilon} \cdot \vec{r} = \sqrt{\frac{4\pi}{3}} r \sum_{q=(0,\pm 1)} \epsilon_q Y_1^q, \quad (21)$$

where the polarization component is $q = 0$ for linear polarization; $q = 1$ for right-handed circular polarization; and $q = -1$ for left-handed polarization of the laser's electric field [42]. The orientation of the laser electric field defines the orientation of the z axis in the spherical coordinate system imposed on the nucleus of a Kr atom.

To evaluate the reduced matrix elements D_{ij} , a simplified expression must first be obtained. By applying the Wigner-Eckart Theorem [42], D_{ij} may be rewritten as

$$\begin{aligned} D_{ij} &= \langle i | \hat{\epsilon} \cdot \vec{r} | j \rangle \\ &= \langle \mathbf{n}_i L_i S_i J_i M_i | \hat{\epsilon} \cdot \vec{r} | \mathbf{n}_j L_j S_j J_j M_j \rangle \\ &= \langle \mathbf{n}_i L_i S_i J_i | \vec{r} | \mathbf{n}_j L_j S_j J_j \rangle \\ &\quad \times \sum_{q=(0,\pm 1)} \epsilon_q \begin{pmatrix} J_i & 1 & J_j \\ -M_i & q & M_j \end{pmatrix} (-1)^{1-J_j-M_i}. \end{aligned} \quad (22)$$

By using the definition of a vector $\vec{r} = r \hat{\epsilon}_r$, radial coordinates are separated from angular coordinates:

$$\begin{aligned} D_{ij} &= \langle i | r | j \rangle \langle L_i S_i J_i | \hat{\epsilon}_r | L_j S_j J_j \rangle \\ &\quad \times \sum_{q=(0,\pm 1)} \epsilon_q \begin{pmatrix} J_i & 1 & J_j \\ -M_i & q & M_j \end{pmatrix} (-1)^{1-J_j-M_i}. \end{aligned} \quad (23)$$

Using the following expression from Messiah {[42] (Eq. C.89)} for reduced matrix elements and irreducible tensor operators of tensor rank k ,

$$\begin{aligned} & \langle \tau_1 \tau_2 J_1 J_2 J | T^{(k)} | \tau_1' \tau_2' J_1' J_2' J' \rangle \\ &= \delta_{\tau_1 \tau_2'} \delta_{J_2 J_2'} \langle \tau_1 J_1 | T^{(k)} | \tau_1' J_1' \rangle (-1)^{J'+J_1+J_2+2} \\ & \times \sqrt{(2J+1)(2J'+1)} \begin{Bmatrix} J_1 & k & J_1' \\ J' & J_2 & J \end{Bmatrix}, \end{aligned} \quad (24)$$

the angular term $\langle L_i S_i J_i | \hat{e}_r | L_j S_j J_j \rangle$ can be further simplified, noting $\tau_1 = \tau_1' = \tau_2 = \tau_2' = 1$. The reduced matrix element D_{ij} becomes

$$\begin{aligned} D_{ij} &= \delta_{S_i S_j} \langle r | \langle L_i | \hat{e}_r | L_j \rangle (-1)^{L_i+J_j+S_i+1} \\ & \times \sqrt{(2J_i+1)(2J_j+1)} \begin{Bmatrix} L_i & 1 & L_j \\ J_j & S_j & J_i \end{Bmatrix} \\ & \times \sum_{q=(0,\pm 1)} \epsilon_q \begin{pmatrix} J_i & 1 & J_j \\ -M_i & q & M_j \end{pmatrix} (-1)^{1-J_j-M_i}, \end{aligned} \quad (25)$$

where $\langle r \rangle = \langle i | r | j \rangle$ is the purely radial matrix element. The term $\delta_{S_i S_j}$ implies that the dipole moment operator does not act on electron coordinates. Next, using the Wigner–Eckart theorem [42] for the expected value of a spherical tensor Y_k of rank k ,

$$\langle l_1 | Y_k | l_2 \rangle = (-1)^{l_1} \sqrt{\frac{(2l_1+1)(2k+1)(2l_2+1)}{4\pi}} \begin{pmatrix} l_1 & k & l_2 \\ 0 & 0 & 0 \end{pmatrix}, \quad (26)$$

the expected value of the rank-1 unit vector, \hat{e}_r , $\langle L_i | \hat{e}_r | L_j \rangle$, can be evaluated. D_{ij} becomes

$$\begin{aligned} D_{ij} &= \delta_{S_i S_j} \langle r \rangle \sqrt{(2L_i+1)(2L_j+1)} \\ & \times \begin{pmatrix} L_i & 1 & L_j \\ 0 & 0 & 0 \end{pmatrix} \sqrt{(2J_i+1)(2J_j+1)} \\ & \times (-1)^{2L_i+J_j+S_i+1} \begin{Bmatrix} L_i & 1 & L_j \\ J_j & S_j & J_i \end{Bmatrix} \\ & \times \sum_{q=(0,\pm 1)} \epsilon_q \begin{pmatrix} J_i & 1 & J_j \\ -M_i & q & M_j \end{pmatrix} (-1)^{1-J_j-M_i}, \end{aligned} \quad (27)$$

which rearranges into

$$\begin{aligned} D_{ij} &= \delta_{S_i S_j} \langle r \rangle \sqrt{(2J_i+1)(2J_j+1)(2L_i+1)(2L_j+1)} \\ & \times \begin{pmatrix} L_i & 1 & L_j \\ 0 & 0 & 0 \end{pmatrix} \begin{Bmatrix} L_i & 1 & L_j \\ J_j & S_j & J_i \end{Bmatrix} (-1)^{2L_i+J_j+S_i+1} \\ & \times \sum_{q=(0,\pm 1)} \epsilon_q \begin{pmatrix} J_i & 1 & J_j \\ -M_i & q & M_j \end{pmatrix} (-1)^{1-J_j-M_i}. \end{aligned} \quad (28)$$

For allowable dipole transitions, the effect of the factor of $-1^{-J_j-M_i+1}$, which arises from the definition of the Wigner–Eckart Theorem, has no effect on the transition matrix element summation due to the consistent parity of J , as shown in Table 1.

The 2×3 matrix terms in parentheses are $3j$ -Wigner symbols, and the 2×3 matrix term in brackets is the $6j$ -Wigner

Table 1. Parity Table for Term^{a,b}

J_j	0		1		2	
M_i	0	1	0	-2	0	3
$-1^{-J_j-M_i+1}$	-1	1	1	1	-1	1

^a $-1^{-J_j-M_i+1}$ $J_j = 0, 1$ corresponds to two-photon transitions, and $J_j = 0, 1, 2$ corresponds to three-photon transitions.

^bThe term $-1^{-J_j-M_i+1}$ does not contribute to the transition matrix element summation because it is consistently the same value for each stage of a multi-photon transition for all possible pathways.

Table 2. Addition of the Angular Momentum of Two Electrons l_1 and: $\vec{L} = \vec{l}_1 + \vec{l}_2$ ($m = 0$ for both electrons)

State	$L^2 = l_1^2 + l_2^2 + 2\vec{l}_1 \cdot \vec{l}_2$	L	J
$ g\rangle$	$1^2 + 1^2 + 2(1)(-1) = 0$	0	0
$ k\rangle$	$1^2 + 0^2 + 2(1)(0) = 1$	1	1
$ f\rangle$	$1^2 + 1^2 + 2(1)(\pm 1) = \begin{Bmatrix} 4 \\ 0 \end{Bmatrix}$	$\begin{Bmatrix} 2 \\ 0 \end{Bmatrix}$	$\begin{Bmatrix} 2 \\ 0 \end{Bmatrix}$

symbol. $3j$ -Wigner symbols enforce dipole moment selection rules, and the $6j$ -Wigner symbol quantifies the degeneracy of a transition occurring (it amounts to a normalization factor). Our research considers only linear polarization of the laser electric field, $q = 0$, forcing $M_i = M_j = 0$ for all transitions $j \rightarrow i$, $S_i = S_j = 0$ for all transitions because the Kr ground state has a total electron spin of zero, and the dipole moment operator $\hat{e} \cdot \vec{r}$ does not act on electron spin coordinates. L_i is the norm of the addition of two angular momenta, $L_i = |\vec{l}_i + \vec{l}_g|$, which describes the angular momentum coupling between the excited electron and a $4p$ valence electron of opposite electron spin. Since the dipole moment operator does not operate on electron coordinates, it turns out that $L_i = J_i$ for the dipole transitions we analyzed. A sketch summarizing how angular momentum changes during $(2+1)$ -photoionization is shown in Fig. 1, and an angular momentum table is provided in Table 2 to show how to calculate the coupled quantum L from the angular momenta of two electrons, each with an azimuthal quantum number $m = 0$.

Therefore, the simplified dipole matrix element is

$$D_{ij} = \delta_{l_i, l_j \pm 1} \langle r \rangle (2J_i+1)(2J_j+1) \begin{pmatrix} J_i & 1 & J_j \\ 0 & 0 & 0 \end{pmatrix}^2 \begin{Bmatrix} J_i & 1 & J_j \\ J_j & 0 & J_i \end{Bmatrix}, \quad (29)$$

noting that for a dipole transition, $\Delta l = \pm 1$. The factor of $(-1)^{2L_i+J_j+S_i+1}$ is omitted because it does not contribute any meaningful sign change in the summation. For dipole moments, parity is conserved, resulting in consistent state parity. $S_i + 1$ is always one; $2L_i$ is always even; and -1^{J_j} is consistent for all considered transitions. More interestingly, due to the consistent parity of J for transition states, Eq. (29) is symmetric about variable exchange, $i \leftrightarrow j$ which conforms to the symmetry property of a Green's function, Eq. (14). Using identity (C.37) from [42], Eq. (29) can be further simplified to

$$D_{ij} = \delta_{l_i, l_j \pm 1} \langle r \rangle \sqrt{(2J_i+1)(2J_j+1)} \begin{pmatrix} J_i & 1 & J_j \\ 0 & 0 & 0 \end{pmatrix}^2. \quad (30)$$

Now, the main difficulty with calculating D_{ij} is the evaluation of the radial wave function integral $\langle r \rangle$:

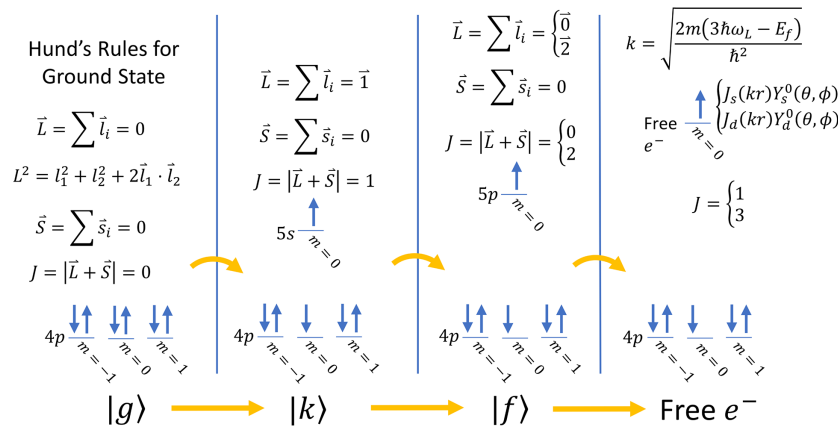


Fig. 1. Angular momenta of a Kr atom during linearly polarized (2 + 1) multiphoton photoionization. This sketch demonstrates LS spin-orbit coupling for each Kr state at each stage of excitation: ground state $|g\rangle$, intermediate state $|k\rangle$, two-photon state $|f\rangle$, and ionized state e^- . For dipole transitions, $\Delta S = 0$ and, consequently, $J = L$.

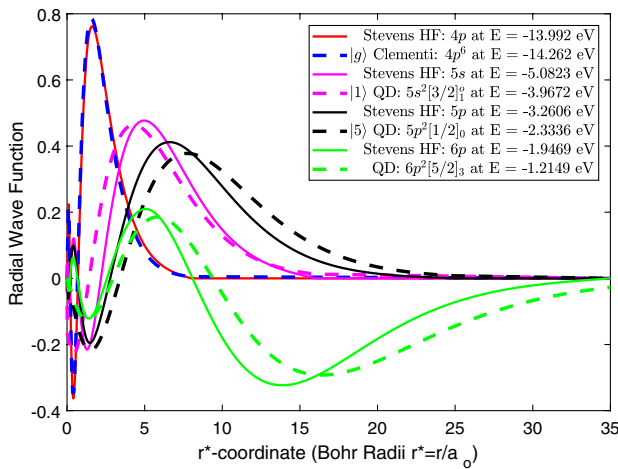


Fig. 2. Comparison between Hartree-Fock (HF) radial orbitals and quantum-defect (QD) radial orbitals. The Clementi $4p$ radial wave is described in [35]. This plot demonstrates the hydrogen-like behavior of Kr radial wave functions. This plot justifies the use of quantum-defect orbitals and validates Rydberg's original observation of the hydrogenic behavior of excited atoms [43].

$$\langle r \rangle = \langle R_i(r) | r | R_j(r) \rangle \prod_p \langle R_{i,p}(r_p) | R_{j,p}(r_p) \rangle$$

$$= \int_0^\infty r^3 R_i(r) R_j(r) dr, \quad (31)$$

because the form of the wave functions $R_i(r)$ must be assumed from prior knowledge. The one-electron model of Kr also assumes that only the radial wave function of the excited electron changes, an assumption justified by a Hartree-Fock calculation [35]. Therefore, $\prod_p \langle R_{i,p}(r_p) | R_{j,p}(r_p) \rangle = 1$ due to the normalization of the radial wave functions.

Excited states of noble gas atoms approximate one-electron atoms, and to first order, electric dipoles. QDT correctly assumes that the excited states of atoms exhibit scaled, hydrogen-like behavior, as verified by our Hartree-Fock calculation shown in Fig. 2. This observation was first made by Rydberg [43] and was later exploited by Bethe *et al.* [37], Bebb *et al.* [44], and McGuire [7,8]. While Hartree-Fock iterates for an explicit electron repulsion potential [35,41], QDT directly

incorporates the effect of electron repulsion through the use of excited state energy as an input to scale the wave function. With the verified assumption of hydrogenic behavior for excited Kr states, quantum-defect radial wave functions can be used with confidence to describe the excited states of Kr.

Properly normalized hydrogen radial wave functions [45] are expressed as

$$R_{nl}(r) = \sqrt{\left[\frac{(n-l-1)!}{2n(n+l)!} \left(\frac{2Z_e}{n} \right)^3 \right]} \left(\frac{2Z_e r}{n} \right)^l$$

$$\times \exp\left(\frac{-Z_e r}{n} \right) L_{n-l-1}^{2l+1} \left(\frac{2Z_e r}{n} \right), \quad (32)$$

with effective nuclear charge $Z_e = 1$ and energy $E_n = -Ry/n^2$. Meanwhile, quantum-defect radial wave functions [43] are scaled hydrogen radial wave functions and are written similarly as

$$R_{nl}(E, I_m, r) = \frac{2}{(n^*)^2} \sqrt{\frac{\Gamma(n-l-I_m(l))}{\Gamma(n^*+l^*+1)}} \left(\frac{2r}{n^*} \right)^l$$

$$\times \exp\left(\frac{-r}{n^*} \right) L_{n-l-I_m(l)-1}^{2l^*+1} \left(\frac{2r}{n^*} \right), \quad (33)$$

where the effective principal quantum number is

$$n^* = n - \delta_d, \quad (34)$$

the quantum defect is

$$\delta_d = n - \sqrt{\frac{-Ry}{E}}, \quad (35)$$

and the effective angular momentum quantum number is

$$l^* = l - \delta_d + I_m(l). \quad (36)$$

Γ is the gamma function; $(!)$ is the factorial function; and $L_n^y(x)$ is the associated Laguerre polynomial function of degree n and input y evaluated at x . Eq. (33) is a scaled version of Eq. (32).

Quantum-defect radial wave functions are generated by four input parameters, n , l , E , and I_m , which are determined by

NIST data [36] and are listed in Table 3 for a basis of Kr states. n and l are reported in the Racah notation of a state. Absolute energy E is obtained by subtracting the first ionization energy of Kr (13.9996053 eV) from the reported NIST energy because NIST reports energy relative to the ground state. For the selection of the integer, I_m Einstein coefficients are used to ensure that the radial wave functions reflect experimental observations. Also, $(\delta_d - l - 1/2) \leq I_m < (n - l - 1)$ [43]. By minimizing the discrepancy between calculated Einstein coefficients [4],

$$A_{ij} = \frac{2e^2\omega_{ij}^3 a_o^2}{3c^3 h \epsilon_o} \sum_{m_j} |(n_i l_i m_i | \vec{r} | n_j l_j m_j)|^2, \quad (37)$$

and tabulated NIST Einstein coefficients through integer variation of I_m , acceptable radial wave functions are constructed for excited Kr states.

The initial state $|i\rangle$ has a degenerate azimuth quantum number m_i . In a pure dipole moment transition, the only active quantum number is the angular momentum quantum number l . Unlike Hillborn [4], a weighted summation must take place over both m_i and m_j to account for the degeneracy of both quantum numbers in an isotropic electric field: $q = 0, \pm 1$. Therefore,

$$\begin{aligned} A_{ij} &= \frac{2e^2\omega_{ij}^3 a_o^2}{3c^3 h \epsilon_o} \sum_{m_i} \frac{1}{\sqrt{w_t}} \sum_{m_j} \sum_{q=0, \pm 1} |(n_i l_i m_i | \vec{r} | n_j l_j m_j)|^2 \\ &= \frac{2e^2\omega_{ij}^3 a_o^2}{3c^3 h \epsilon_o} \left[\langle r \rangle \sqrt{\frac{(2l_i + 1)(2l_j + 1)}{w_t}} \begin{pmatrix} l_i & 1 & l_j \\ 0 & 0 & 0 \end{pmatrix} \right]^2 \\ &= \frac{2e^2\omega_{ij}^3 a_o^2}{3c^3 h \epsilon_o} \left[\langle r \rangle \frac{1}{\sqrt{3}} \right]^2 \quad \text{for } s \leftrightarrow p \text{ transitions} \\ &= \frac{2e^2\omega_{ij}^3 a_o^2}{3c^3 h \epsilon_o} \left[\langle r \rangle \sqrt{\frac{2}{9}} \right]^2 \quad \text{for } p \leftrightarrow d \text{ transitions,} \end{aligned} \quad (38)$$

where w_t is the number of nonzero transitions produced by the degeneracy of m_i and m_j in an isotropic radiation field. $1/w_t$ is the probability of a transition occurring. For fixed l_i and l_j , the value of w_t can be determined from the number of nonzero Clebsch–Gordan coefficients for varying m_i , m_j and polarization component q . For $s \leftrightarrow p$ transitions, $w_t = 3$, and for $p \leftrightarrow d$ transitions, $w_t = 9$. Eq. (38) amounts to practical means to calculate Einstein coefficients from a set of radial wave functions. Results are shown in Table 4. For the ground state $|g\rangle$, a Hartree–Fock radial orbital, composed of a linear combination of Slater-type orbitals (STOs), from Clementi *et al.* [35] is used:

$$\begin{aligned} R_{4p}(r) &= 0.08488 \times \text{STO}(2, 17.03660, r) \\ &+ 0.00571 \times \text{STO}(2, 26.04380, r) \\ &+ 0.04169 \times \text{STO}(3, 15.51000, r) \\ &- 0.07425 \times \text{STO}(3, 9.49403, r) \\ &- 0.26866 \times \text{STO}(3, 6.57275, r) \\ &+ 0.01341 \times \text{STO}(4, 5.38507, r) \\ &+ 0.51241 \times \text{STO}(4, 3.15603, r) \\ &+ 0.42557 \times \text{STO}(4, 2.02966, r) \\ &+ 0.18141 \times \text{STO}(4, 1.42733, r), \end{aligned} \quad (39)$$

where the normalized STO function is defined as

$$\text{STO}(n, \zeta, r) = \frac{1}{\sqrt{(2n)!}} (2\zeta)^{(n+1/2)} r^{n-1} e^{-\zeta r}. \quad (40)$$

This ground-state Hartree–Fock radial wave function assumes a spherically symmetric electric charge distribution and accounts to first order the electron repulsion exerted on a $4p$ electron.

In Table 4, Einstein coefficients are calculated via Eq. (38) with varying accuracy but to the correct order of magnitude. The QDT parameter, I_m , is tuned to maximize the accuracy of A_{ij} . By obtaining the correct order of magnitude and in some cases the correct Einstein coefficient, Table 4 further validates the use of quantum-defect radial wave functions Eq. (33).

With a basis of wave functions calibrated on NIST atomic spectra data, Eqs. (19) and (8) are evaluated directly, producing the two-photon cross-section data shown in Fig. 3. The values of cross-sections are shown in Tables 5–7. When quantum-defect radial wave functions are used in conjunction with OS formulas for linear polarization [3], such as

$$\langle i | \hat{\epsilon} \cdot \vec{r} | j \rangle = \sqrt{\frac{3A_{ij} h c^3 \epsilon_o}{2e^2 \omega_{ij}}} \sqrt{2J_i + 1} \begin{pmatrix} J_i & 1 & J_j \\ 0 & 0 & 0 \end{pmatrix}, \quad (41)$$

good agreement is obtained with the Richardson *et al.* [23] excitation spectrum, especially using basis sets 2 and 3, which include d orbitals.

The resulting approach is a hybrid method for the evaluation of dipole matrix elements, consisting of quantum-defect theory and where possible, OS. Another contribution of quantum-defect theory is the prediction of the sign of the radial matrix element from the evaluation of Eq. (31). The OS, Eq. (41), must retain the same sign as Eq. (31) and Eq. (29). This sign determines which excitation pathways make constructive and destructive contributions to the two-photon transition matrix element. Also, wherever Eq. (41) is used for the evaluation of a matrix element, the equality $D_{ij} = D_{ji}$ must be used to ensure symmetry. This properly interfaces QDT with OS formulas, creating the hybrid dipole matrix element evaluation method and thus allowing for the eventual extension of Eq. (19) to general multiphoton excitation. For example, for three-photon excitation, the entire dipole matrix D is used:

$$M_{fg}^{(3)} = \sum_{k=g}^N \sum_{p=g}^N D_{fk} G_{kk} D_{kp} G_{pp} D_{pg} = \hat{\epsilon}_f^T D G D G D \hat{\epsilon}_g. \quad (42)$$

When using a hybrid dipole matrix element calculation scheme, selection of states with adequate experimental data is crucial for reasonable results. Insufficient transition probability data rendered some state omissions in the finite basis of states listed in Table 3. For example, only one $4d$ orbital state, $|21\rangle$, was used in basis sets 2 and 3 (Tables 6 and 7) because it had the highest observed transition probability of all $4d$ states between itself and ground, and it had the highest experimentally measured transition probability between itself and a $5p$ state: $|21\rangle \rightarrow |10\rangle$. It was the only state with high transition probabilities between $4d$ and $5p$ levels. More importantly, state $|21\rangle$ exhibited dipole-moment behavior, which could be described by quantum-defect theory. The effect of other $4d$ orbitals on the excitation process is small but can be better determined once

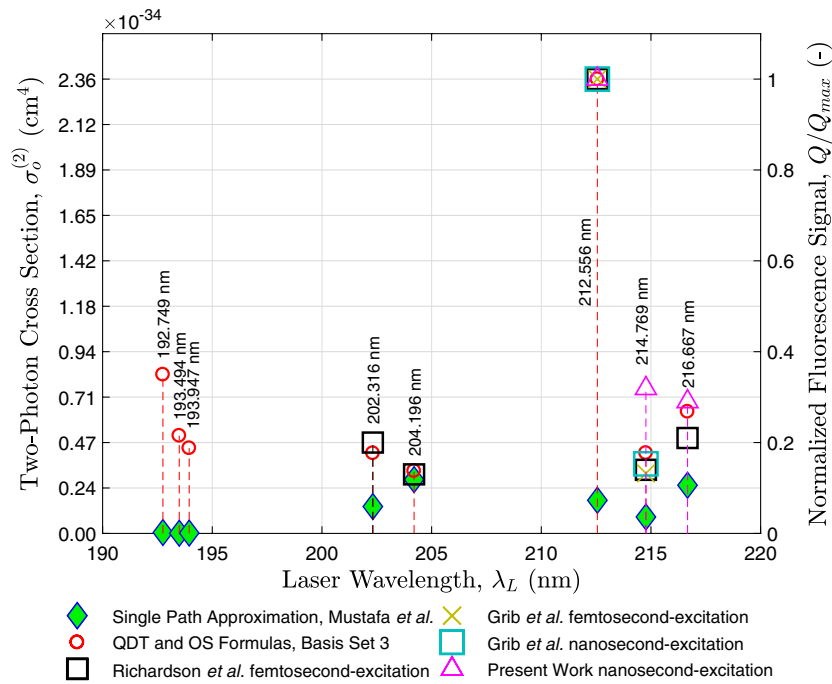


Fig. 3. Two-photon excitation cross-sections using basis set 3 as the basis of intermediate states, which include $5s$, $6s$, $7s$, $4d$, $5d$, and $6d$ states. Via quantum-defect theory (QDT) and oscillator strength formulas, cross-sections were calculated and compared to the excitation data of Richardson *et al.*, Grib *et al.*, and our laboratory. Richardson data were obtained by fs-laser excitation in a 1 bar, 95% Ar/5% gas mixture. Grib data were obtained by both fs-laser and ns-laser excitations in a 1 atm, 77% N_2 /33% Kr gas mixture. Our laboratory data were obtained via ns-laser excitation in a 1 torr, 99% N_2 /1% Kr gas mixture to minimize collisional effects. Calculated cross-sections and normalized experimental excitation data are listed in Appendix A.

more transition probabilities become available for transitions between $4d$ and $5p$ states. However, the inclusion of other $4d$ states will not significantly change the excitation spectrum shown in Fig. 3. The same reasoning was made for the inclusion of $5d$ and $6d$ states in basis set 3.

4. EXPERIMENTAL SETUP

A frequency-doubled Quanta Ray Pro-350 Nd:YAG laser pumping a frequency tripled Sirah PrecisionScan Dye Laser (DCM dye, DMSO solvent) is the approach used for nanosecond excitation in this work. A schematic of the optical setup is shown in Fig. 4. The Nd:YAG laser pumps the dye laser with 1000 mJ/pulse at a wavelength of 532 nm. The dye laser is tuned to output a 637.67/644.31/650.01 nm beam and

frequency tripling (Sirah THU 205) of the dye laser output results in a 212.56/214.77/216.67 nm beam, with 3 mJ energy, 1350 MHz linewidth, and 7 ns pulsewidth at a repetition rate of 10 Hz. The write beam was focused into the test cell with a 200 mm focal length, fused-silica lens. The beam fluence and spectral intensity at the waist were $1.28 \times 10^4 \text{ J/cm}^2$ and $1.35 \times 10^3 \text{ W/(cm}^2\text{Hz)}$, respectively. The intensified CCD camera used for all experiments was a Princeton Instruments PIMAX-4 (PM4-1024i-HR-FG-18-P46-CM) with a Nikon NIKKOR 24-85 mm f/2.8-4D lens in “macro” mode and positioned approximately 200 mm from the excitation location. Excitation was performed for three different wavelengths and the fluorescence signal was recorded at the rising edge of the excitation process, as shown in Fig. 3.

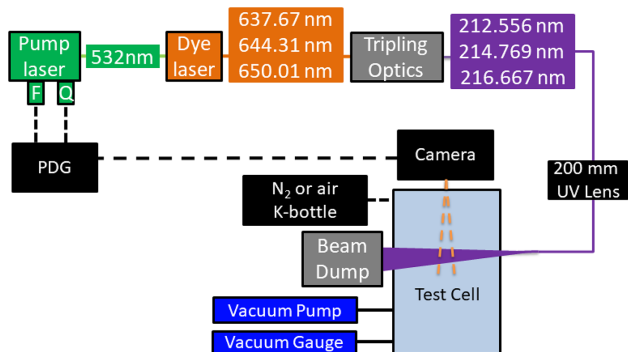


Fig. 4. Schematic of experimental setup. PDG, pulse delay generator.

5. COMPARISON OF TWO-PHOTON CROSS-SECTION CALCULATION WITH EXPERIMENT

Cross-section calculations are reported for eight excitation lines (192.749 nm, 193.494 nm, 193.947 nm, 202.316 nm, 204.196 nm, 212.556 nm, 214.769 nm, 216.667 nm) in Tables 5–7 for basis sets 1, 2, and 3, respectively; these cross-section calculations are compared to three sets of excitation spectrum data in Fig. 3 with good agreement. The first experimental data set is from the previously discussed nanosecond excitation at 212.556 nm, 214.769 nm, and 216.667 nm. Excitation lines at lower wavelengths with the setup are not

currently accessible. Additionally, we present the Richardson *et al.* [23] excitation spectrum from a femtosecond excitation at 202.316 nm, 204.196 nm, 212.556 nm, 214.769 nm, and 216.667 nm. This spectrum approximates the impulse/natural response of the Kr atom. Due to the short timescales of excitation of Richardson *et al.* [23], and due to the closely clustered energies of eight, two-photon excited krypton states, the two-photon cross-section can be compared directly to the fluorescence results. The plotted, relative fluorescence signal magnitudes for 212.556 nm and 214.769 nm excitation of Grib *et al.* [24] also agree with both the Richardson *et al.* [23] excitation spectrum and our excitation spectrum, regardless of fs- or ns-laser excitation. Normalized experimental excitation data are listed in Table 8 for all considered data sets. In Fig. 4, comparison is also made to the single-path approximation, whose cross-section values are listed in Table 9. Single-path approximation is unable to reconstruct the experimentally observed excitation spectrum, but it can obtain rough estimates of cross-sections.

The convergence of the summation over the intermediate basis set $|k\rangle$ is shown in Tables 5–7, which agrees with the convergence criterion of Eq. (13): $n_{\max} \leq 7$.

In Table 7, the calculated cross-section for 214.769 nm excitation is $4.18 \times 10^{-35} \text{ cm}^4$. This cross-section agrees well with the experimentally measured 214.769 nm two-photon cross-section of Dakka *et al.* [46]: $5.2 \pm 2.2 \times 10^{-35} \text{ cm}^4$. This validates the order of magnitude of calculated cross-sections for basis set 3.

Overall, the comparison of the calculated two-photon cross-sections with the experimental data of multiple research groups is good for lines between 200 and 220 nm. Cross-sections for lines between 190 and 200 nm are predictions calculated by the method described within this paper.

6. CONCLUSION

This paper presents multi-path, two-photon excitation cross-section calculations for krypton that compare well to experiment for lines between 200 and 220 nm. Cross-sections were also calculated for excitation wavelengths lying between 190 and 200 nm.

To make these calculations, a hybrid method was used, consisting of OSs, and where those are unlisted in the NIST data, QDT to evaluate reduced matrix elements $\langle \vec{r} \rangle$ and purely radial matrix elements $\langle r \rangle$. QDT was used to predict the sign of tabulated and calculated OSs from NIST. Including the transition pathways unlisted in the NIST data was key to increasing the accuracy of the calculation. These pathways were constructed from a finite basis of states consisting of $4p$, $5s$, $6s$, $7s$, $5p$, $6p$, $4d$, $5d$, and $6d$ orbitals.

The two-photon cross-section analysis revealed the symmetric behavior of the transition matrix element $M_{fg}^{(2)}$ with respect to variable exchange $f \leftrightarrow g$; the symmetric behavior

of the reduced matrix element $\langle i | \hat{\epsilon} \cdot \vec{r} | j \rangle$ with respect to index exchange $i \leftrightarrow j$; and the hydrogenic behavior of the excited states of Kr.

Most importantly, this work provides a fundamental physical understanding in identifying the optimal Kr fluorescence excitation line (i.e., Kr-PLIF or KTV). From this work, and the successful comparison to experiment from our laboratory and those in the literature, we conclude that the optimal line is 212.556 nm for Kr-PLIF and single-laser KTV. Note that two-laser KTV has an optimal write-laser excitation of 216.667 nm, but the supporting details for that assertion are not included here for brevity.

APPENDIX A: TABLES OF ATOMIC DATA, INPUT PARAMETERS, AND CALCULATION RESULTS

Here, we provide data tables (Tables 3 and 4) for krypton states and input parameters from which to form Kr radial wave functions, and calculation result tables in Tables 5–7 that justify

Table 3. Input Parameters for Quantum-Defect Radial Wave Functions^{a,b,c}

Index	State (Term Symbol) ^d	n	l	E (eV)	I_m	λ_L (nm)
G	$4p^6 1S_0$	4	1	-13.9996053	–	–
1	$(^2P_{3/2}^o)5s^2[3/2]_1^o$	5	0	-3.96720476	3	–
2	$(^2P_{3/2}^o)5s^2[3/2]_2^o$	5	0	-4.08437309	2	–
3	$(^2P_{1/2}^o)5s^2[1/2]_1^o$	5	0	-3.35597053	3	–
4	$(^2P_{1/2}^o)5s^2[1/2]_0^o$	5	0	-3.43719109	2	–
5	$(^2P_{3/2}^o)5p^2[1/2]_0$	5	1	-2.33357724	3	212.556
6	$(^2P_{3/2}^o)5p^2[3/2]_2$	5	1	-2.45378261	1	214.769
7	$(^2P_{3/2}^o)5p^2[1/2]_1$	5	1	-2.69615013	2	219.374
8	$(^2P_{3/2}^o)5p^2[5/2]_3$	5	1	-2.55655804	3	216.698
9	$(^2P_{3/2}^o)5p^2[5/2]_2$	5	1	-2.55494904	1	216.667
10	$(^2P_{3/2}^o)5p^2[3/2]_1$	5	1	-2.47348948	1	215.136
11	$(^2P_{1/2}^o)5p^2[3/2]_2$	5	1	-1.85595245	2	204.196
12	$(^2P_{1/2}^o)5p^2[1/2]_0$	5	1	-1.74313881	2	202.316
13	$(^2P_{1/2}^o)5p^2[1/2]_1$	5	1	-1.85917847	1	204.250
14	$(^2P_{1/2}^o)5p^2[3/2]_1$	5	1	-1.89925407	1	204.927
15	$(^2P_{3/2}^o)6p^2[1/2]_0$	6	1	-1.13480243	3	192.749
16	$(^2P_{3/2}^o)6p^2[3/2]_2$	6	1	-1.18427475	3	193.494
17	$(^2P_{3/2}^o)6p^2[5/2]_2$	6	1	-1.21421328	2	193.947
18	$(^2P_{1/2}^o)6s^2[1/2]_1$	6	0	-0.963121959	2	–
19	$(^2P_{3/2}^o)6s^2[3/2]_1$	6	0	-1.614321866	1	–
20	$(^2P_{1/2}^o)7s^2[1/2]_1$	7	0	-0.885709772	1	–
21	$(^2P_{3/2}^o)4d^2[3/2]_1$	4	2	-1.645049675	1	–
22	$(^2P_{3/2}^o)5d^2[1/2]_1$	5	2	-1.129823313	2	–
23	$(^2P_{3/2}^o)6d^2[3/2]_1$	6	2	-0.577230406	1	–
24	$(^2P_{3/2}^o)6d^2[1/2]_1$	6	2	-0.649464393	3	–

^aThis table also provides the basis of states used to calculate two-photon transition matrix element. Data were obtained from NIST [36].

^bStates [5], [6], [9], [11], [12], [15], [16], and [17] are of critical interest for the laser excitation lines considered in this paper.

^cThe λ_L column lists the laser excitation wavelength required for two-photon excitation, as measured in vacuum.

^dTwo notations were used. (1) For the Kr ground state, Russell–Saunders $^{2S+1}L_J$ notation is used (LS coupling). (2) For excited Kr states, Racah $(^{2S_1+1}P_{J_1}^o)nl^{(2S_1+1)}[K]_J^o$ notation is used (LS_1 coupling). $\vec{J} = \vec{K} + \vec{s}$ and $\vec{K} = \vec{L} + \vec{S}_1$ [36]. S_1 is the total electron spin of the ion, s is the spin of the excited electron, and L is the total orbital angular momentum. $\vec{S} = \vec{S}_1 + \vec{s}$.

Table 4. Calculation of Einstein Coefficients Using Quantum-Defect Functions and Comparison with NIST Experimental Data^a [36]

Transition $ i\rangle \rightarrow j\rangle$	NIST			Quantum-Defect Theory	
	λ_{ij} (nm)	A_{ij} (1/s)	Acc. 3	A_{ij} (1/s)	% Error
$ 23\rangle \rightarrow g\rangle$	92.3713	1.14×10^8	C	4.16×10^7	63.0%
$ 24\rangle \rightarrow g\rangle$	92.8711	3.87×10^6	C	2.64×10^5	93.2%
$ 22\rangle \rightarrow g\rangle$	96.3374	3.35×10^7	C	2.13×10^7	36.3%
$ 20\rangle \rightarrow g\rangle$	94.5441	2.81×10^8	C	1.0450×10^8	62.8%
$ 18\rangle \rightarrow g\rangle$	95.1056	2.58×10^7	C	6.8928×10^7	167.2%
$ 19\rangle \rightarrow g\rangle$	100.1061	3.42×10^8	C	2.68×10^8	21.5%
$ 21\rangle \rightarrow g\rangle$	100.3550	1.82×10^8	C	1.37×10^8	24.8%
$ 3\rangle \rightarrow g\rangle$	116.4867	3.09×10^8	A+	2.33×10^8	24.5%
$ 1\rangle \rightarrow g\rangle$	123.5838	2.98×10^8	A+	4.97×10^8	66.7%
$ 15\rangle \rightarrow 2\rangle$	427.5172	1.99×10^6	C+	1.74×10^6	12.7%
$ 16\rangle \rightarrow 1\rangle$	437.7351	3.74×10^6	B	2.45×10^6	34.4%
$ 15\rangle \rightarrow 1\rangle$	445.5168	3.97×10^5	B	4.92×10^5	23.9%
$ 17\rangle \rightarrow 1\rangle$	450.3617	7.8×10^5	C	4.59×10^6	488.7%
$ 5\rangle \rightarrow 1\rangle$	758.7414	4.310×10^7	A+	4.77×10^7	10.8%
$ 6\rangle \rightarrow 2\rangle$	760.1546	2.732×10^7	AA	2.78×10^7	1.8%
$ 12\rangle \rightarrow 3\rangle$	768.7361	4.064×10^7	AA	2.98×10^7	26.8%
$ 10\rangle \rightarrow 2\rangle$	769.6658	4.27×10^6	A	2.74×10^7	540.9%
$ 13\rangle \rightarrow 4\rangle$	785.6984	2.041×10^7	A	2.14×10^7	5.0%
$ 14\rangle \rightarrow 4\rangle$	806.1721	1.583×10^7	B+	2.19×10^7	38.6%
$ 8\rangle \rightarrow 2\rangle$	811.5132	3.610×10^7	AAA	3.50×10^7	3.10%
$ 6\rangle \rightarrow 1\rangle$	819.2308	8.94×10^6	A	2.75×10^7	207.3%
$ 11\rangle \rightarrow 3\rangle$	826.5514	3.416×10^7	AA	2.93×10^7	14.2%
$ 9\rangle \rightarrow 1\rangle$	877.9161	2.217×10^7	AA	2.43×10^7	9.66%
$ 7\rangle \rightarrow 3\rangle$	893.1145	2.289×10^7	A	2.24×10^7	2.02%

^aNIST estimated accuracy of Einstein coefficient. AAA $\leq 0.3\%$, AA $\leq 1\%$, A $\leq 3\%$, B+ $\leq 7\%$, B $\leq 10\%$, C+ $\leq 18\%$, C $\leq 25\%$.

Table 5. Two-Photon Cross-Sections Using Basis Set 1: 5s, 6s, and 7s States

Basis	Basis Set 1: $ g\rangle, 1\rangle, 2\rangle, \dots 20\rangle$					
	Theory	Quantum-Defect			Quantum-Defect with Oscillator Strengths	
λ_L (nm)	$\sigma_o^{(2)}$ (cm ⁴)	$\sigma^{(2)} = \sigma_o^{(2)} g(2\omega_L)$ (cm ⁴ · s)	$\frac{\sigma^{(2)}}{\ \sigma^{(2)}\ _\infty}$	$\sigma_o^{(2)}$ (cm ⁴)	$\sigma^{(2)} = \sigma_o^{(2)} g(2\omega_L)$ (cm ⁴ · s)	$\frac{\sigma^{(2)}}{\ \sigma^{(2)}\ _\infty}$
192.749	7.02×10^{-37}	2.29×10^{-47}	0.005	1.73×10^{-36}	5.65×10^{-47}	0.016
193.494	5.01×10^{-37}	1.64×10^{-47}	0.003	3.70×10^{-38}	1.21×10^{-48}	0.0003
193.947	7.28×10^{-37}	2.39×10^{-47}	0.005	1.25×10^{-37}	4.10×10^{-48}	0.001
202.316	2.17×10^{-35}	7.39×10^{-46}	0.151	6.67×10^{-37}	2.27×10^{-47}	0.006
204.196	2.55×10^{-35}	8.74×10^{-46}	0.178	3.84×10^{-37}	1.32×10^{-47}	0.004
212.556	1.39×10^{-34}	4.91×10^{-45}	1.000	1.03×10^{-34}	3.63×10^{-45}	1.000
214.769	5.56×10^{-35}	1.98×10^{-46}	0.404	3.30×10^{-35}	1.18×10^{-45}	0.324
216.667	6.23×10^{-35}	2.24×10^{-46}	0.455	3.92×10^{-35}	1.41×10^{-45}	0.388

Table 6. Two-Photon Cross-Sections Using Only Basis Set 2: 5s, 6s, 7s, and 4d States

Basis	Basis Set 2: $ g\rangle, 1\rangle, 2\rangle, \dots 21\rangle$					
	Theory	Quantum-Defect			Quantum-Defect with Oscillator Strengths	
λ_L (nm)	$\sigma_o^{(2)}$ (cm ⁴)	$\sigma^{(2)} = \sigma_o^{(2)} g(2\omega_L)$ (cm ⁴ · s)	$\frac{\sigma^{(2)}}{\ \sigma^{(2)}\ _\infty}$	$\sigma_o^{(2)}$ (cm ⁴)	$\sigma^{(2)} = \sigma_o^{(2)} g(2\omega_L)$ (cm ⁴ · s)	$\frac{\sigma^{(2)}}{\ \sigma^{(2)}\ _\infty}$
192.749	2.56×10^{-35}	8.37×10^{-46}	0.094	2.80×10^{-35}	9.15×10^{-46}	0.133
193.494	9.85×10^{-35}	7.42×10^{-46}	0.084	1.60×10^{-35}	5.26×10^{-46}	0.077
193.947	1.73×10^{-35}	5.67×10^{-46}	0.064	1.20×10^{-35}	3.93×10^{-46}	0.057
202.316	1.04×10^{-34}	3.55×10^{-45}	0.400	1.95×10^{-35}	6.61×10^{-46}	0.0963
204.196	9.85×10^{-35}	3.37×10^{-45}	0.381	1.57×10^{-35}	5.39×10^{-46}	0.0784
212.556	2.51×10^{-34}	8.86×10^{-45}	1.000	1.94×10^{-34}	6.87×10^{-45}	1.000
214.769	1.32×10^{-34}	4.71×10^{-45}	0.531	3.95×10^{-35}	1.41×10^{-45}	0.205
216.667	1.38×10^{-34}	4.95×10^{-45}	0.559	6.34×10^{-35}	2.28×10^{-45}	0.331

Table 7. Two-Photon Cross-Sections Using Only Basis Set 3: 5s, 6s, 7s, 4d, 5d, and 6d States

Theory	Basis Set 3: $ g\rangle, 1\rangle, 2\rangle, \dots 24\rangle$					
	Quantum-Defect			Quantum-Defect with Oscillator Strengths		
λ_L (nm)	$\sigma_o^{(2)}$ (cm ⁴)	$\sigma^{(2)} = \sigma_o^{(2)} g(2\omega_L)$ (cm ⁴ · s)	$\frac{\sigma^{(2)}}{\ \sigma^{(2)}\ _\infty}$	$\sigma_o^{(2)}$ (cm ⁴)	$\sigma^{(2)} = \sigma_o^{(2)} g(2\omega_L)$ (cm ⁴ · s)	$\frac{\sigma^{(2)}}{\ \sigma^{(2)}\ _\infty}$
192.749	6.53×10^{-35}	2.13×10^{-45}	0.206	8.25×10^{-35}	2.70×10^{-45}	0.323
193.494	5.31×10^{-35}	1.74×10^{-45}	0.198	5.08×10^{-35}	1.66×10^{-45}	0.199
193.947	4.46×10^{-35}	1.47×10^{-45}	0.142	4.43×10^{-35}	1.45×10^{-45}	0.174
202.316	1.46×10^{-34}	4.96×10^{-45}	0.479	4.17×10^{-35}	1.42×10^{-45}	0.170
204.196	1.32×10^{-34}	4.53×10^{-45}	0.438	3.25×10^{-35}	1.11×10^{-45}	0.133
212.556	2.92×10^{-34}	1.03×10^{-44}	1.000	2.36×10^{-34}	8.34×10^{-45}	1.000
214.769	1.62×10^{-34}	5.79×10^{-45}	0.559	4.18×10^{-35}	1.49×10^{-45}	0.179
216.667	1.67×10^{-34}	6.01×10^{-45}	0.581	6.33×10^{-35}	2.27×10^{-45}	0.272

Table 8. Experimental Kr Excitation Signal Normalized Against 212.556 nm Excitation Signal

λ_L (nm)	202.316	204.196	212.556	214.769	216.667
Richardson <i>et al.</i> fs-excitation	0.20	0.13	1.00	0.21	(–)
Grib <i>et al.</i> fs-excitation	(–)	(–)	1.00	0.153	(–)
Grib <i>et al.</i> ns-excitation	(–)	(–)	1.00	0.132	(–)
Present work ns-excitation	(–)	(–)	1.00	0.319	0.290

Table 9. Single-Path Approximation Calculations

λ_L (nm)	State $ k\rangle$	State $ f\rangle$	$\sigma_o^{(2)}$ (cm ⁴)	$\sigma^{(2)}$ (cm ⁴ · s)	$\frac{\sigma^{(2)}}{\ \sigma^{(2)}\ _\infty}$
192.749	$ 1\rangle$	$ 15\rangle$	4.73×10^{-37}	1.55×10^{-47}	0.016
193.494	$ 1\rangle$	$ 16\rangle$	1.04×10^{-37}	3.40×10^{-48}	0.004
193.947	$ 1\rangle$	$ 17\rangle$	2.01×10^{-37}	6.60×10^{-48}	0.007
202.316	$ 3\rangle$	$ 12\rangle$	1.40×10^{-35}	4.75×10^{-46}	0.496
204.196	$ 3\rangle$	$ 11\rangle$	2.80×10^{-35}	9.57×10^{-46}	1.000
212.556	$ 1\rangle$	$ 5\rangle$	1.72×10^{-35}	6.08×10^{-46}	0.635
214.769	$ 1\rangle$	$ 6\rangle$	8.54×10^{-35}	3.05×10^{-46}	0.318
216.667	$ 1\rangle$	$ 9\rangle$	2.50×10^{-35}	8.98×10^{-46}	0.939

our choice of basis for the two-photon excitation of krypton in the 190–220 nm range. For comparison to our calculated cross-section results, we also tabulate experimental excitation fluorescence, obtained in our lab and the literature, in Table 8, and we tabulate single-path approximation results in Table 9.

Funding. Office of Naval Research (N00014-19-1-2523, N00014-20-1-2549, N00014-20-1-2637, N00014-20-1-2682); U.S. Air Force Office of Scientific Research (FA9550-18-1-0403, FA2487-19-C-0013).

Acknowledgment. We acknowledge the helpful consultation of Professors Vladimir Lukic and Kevin Connington on theoretical and numerical matters, such as the evaluation of reduced matrix elements and the use of the spectral-shifted inverse power method in the Hartree–Fock method.

Disclosures. The authors declare no conflicts of interest.

REFERENCES

- P. Lambropoulos, "Topics on multiphoton processes in atoms," *Adv. At. Mol. Phys.* **12**, 87–164 (1976).
- N. M. Khambatta, J. A. Oertel, R. Silk, L. J. Radziemski, and J. M. Mack, "Absolute excited state and ion densities from two- and three-photon processes in some 6p levels of atomic krypton," *J. Appl. Phys.* **64**, 4809–4814 (1988).
- N. M. Khambatta, L. J. Radziemski, and S. N. Dixit, "Upper bound for a three-photon excitation cross section in atomic argon in the ultraviolet regime," *Phys. Rev. A* **39**, 3842–3845 (1989).
- R. C. Hillborn, "Einstein coefficients, cross sections, f values, dipole moments, and all that," *Am. J. Phys.* **50**, 982–986 (1981).
- J. Bokor, J. Y. Zavelovich, and C. K. Rhodes, "Multiphoton ultraviolet spectroscopy of some 6p levels in krypton," *Phys. Rev. A* **21**, 1453–1459 (1980).
- M. A. Mustafa, D. Shektman, and N. J. Parziale, "Single-laser krypton tagging velocimetry investigation of supersonic air and N₂ boundary-layer flows over a hollow cylinder in a shock tube," *Phys. Rev. Appl.* **11**, 064013 (2019).
- E. J. McGuire, "Green's-function approach to nonresonance multiphoton absorption in the alkali-metal atoms," *Phys. Rev. A* **23**, 186–200 (1981).
- E. J. McGuire, "Two- and three-photon ionization in the noble gases," *Phys. Rev. A* **24**, 835–848 (1981).
- M. E. Casida and M. Huix-Rotllant, "Progress in time-dependent density functional theory," *Annu. Rev. Phys. Chem.* **63**, 287–323 (2012).
- P. G. Burke, P. Francken, and C. J. Joachain, "R-matrix-floquet theory of multiphoton processes," *Europhys. Lett.* **13**, 617–622 (1990).
- P. M. Danehy, J. Weisberger, C. Johansen, D. Reese, T. Fahringer, N. J. Parziale, C. Dedic, J. Estevadeordal, and B. A. Cruden, "Non-intrusive measurement techniques for flow characterization of hypersonic wind tunnels," *Flow Characterization and Modeling of Hypersonic Wind Tunnels (NATO Science and Technology Organization Lecture Series STO-AVT 325), (NF1676L-31725)*, Brussels, Belgium (Von Karman Institute, 2018).
- C. A. Whitehead, B. D. Cannon, and J. F. Wacker, "Trace detection of krypton using laser-induced fluorescence," *Appl. Opt.* **34**, 3250–3256 (1995).
- V. Narayanaswamy, R. Burns, and N. T. Clemens, "Kr-PLIF for scalar imaging in supersonic flows," *Opt. Lett.* **36**, 4185–4187 (2011).
- A. G. Hsu, V. Narayanaswamy, N. T. Clemens, and J. H. Frank, "Mixture fraction imaging in turbulent non-premixed flames with two-photon LIF of krypton," *Proc. Combust. Inst.* **33**, 759–766 (2011).
- O. R. H. Buxton, R. A. Burns, and N. T. Clemens, "Simultaneous krypton PLIF, LII and PIV measurements in a sooting jet flame," *Proceedings of 51st AIAA Aerospace Sciences Meeting including the New Horizons Forum and Aerospace Exposition*, Grapevine, Texas (AIAA 2013).
- O. Park, R. A. Burns, O. H. R. Buxton, and N. T. Clemens, "Mixture fraction, soot volume fraction, and velocity imaging in the soot-inception region of a turbulent non-premixed jet flame," *Proc. Combust. Inst.* **36**, 899–907 (2017).

17. D. Zelenak and V. Narayanaswamy, "Composition-independent mean temperature measurements in laminar diffusion flames using spectral lineshape information," *Exp. Fluids* **58**, 147 (2017).
18. A. Sahoo and V. Narayanaswamy, "Two-dimensional temperature field imaging in laminar sooting flames using a two-line Kr PLIF approach," *Appl. Phys. B* **125**, 168 (2019).
19. D. Zelenak and V. Narayanaswamy, "Demonstration of a two-line Kr PLIF thermometry technique for gaseous combustion applications," *Opt. Lett.* **44**, 367–370 (2019).
20. K. Niemi, V. Der Gathen, and H. F. Döbele, "Absolute calibration of atomic density measurements by laser-induced fluorescence spectroscopy with two-photon excitation," *J. Phys. D* **34**, 2330 (2001).
21. J. B. Schmidt, S. Roy, W. D. Kulatilaka, I. Shkurenkov, I. V. Adamovich, W. R. Lempert, and J. R. Gord, "Femtosecond, two-photon-absorption, laser-induced-fluorescence (fs-TALIF) imaging of atomic hydrogen and oxygen in non-equilibrium plasmas," *J. Phys. D* **50**, 015204 (2016).
22. Y. Wang, C. Capps, and W. D. Kulatilaka, "Femtosecond two-photon laser-induced fluorescence of krypton for high-speed flow imaging," *Opt. Lett.* **42**, 711–714 (2017).
23. D. R. Richardson, N. Jiang, H. U. Stauffer, S. P. Kearney, S. Roy, and J. R. Gord, "Mixture-fraction imaging at 1 kHz using femtosecond laser-induced fluorescence of krypton," *Opt. Lett.* **42**, 3498–3501 (2017).
24. S. W. Grib, P. S. Hsu, H. U. Stauffer, C. D. Carter, and S. Roy, "Comparison of femtosecond and nanosecond two-photon-absorption laser-induced fluorescence of krypton," *Appl. Opt.* **58**, 7621–7627 (2019).
25. S. W. Grib, P. S. Hsu, N. Jiang, J. J. Felver, S. A. Schumaker, C. D. Carter, and S. Roy, "100 kHz krypton planar laser-induced fluorescence imaging," *Opt. Lett.* **45**, 3832–3835 (2020).
26. J. L. Mills, C. I. Sukenik, and R. J. Balla, "Hypersonic wake diagnostics using laser induced fluorescence techniques," *Proceedings of 42nd AIAA Plasmadynamics and Lasers Conference*, Honolulu, Hawaii (AIAA 2011).
27. R. J. Balla and J. L. Everhart, "Rayleigh scattering density measurements, cluster theory, and nucleation calculations at mach 10," *AIAA J.* **50**, 698–707 (2012).
28. N. J. Parziale, M. S. Smith, and E. C. Marineau, "Krypton tagging velocimetry of an underexpanded jet," *Appl. Opt.* **54**, 5094–5101 (2015).
29. D. Zahradka, N. J. Parziale, M. S. Smith, and E. C. Marineau, "Krypton tagging velocimetry in a turbulent mach 2.7 boundary layer," *Exp. Fluids* **57**, 62 (2016).
30. M. A. Mustafa, N. J. Parziale, M. S. Smith, and E. C. Marineau, "Nonintrusive freestream velocity measurement in a large-scale hypersonic wind tunnel," *AIAA J.* **55**, 3611–3616 (2017).
31. M. A. Mustafa, N. J. Parziale, M. S. Smith, and E. C. Marineau, "Amplification and structure of streamwise-velocity fluctuations in four shock-wave/turbulent boundary-layer interactions," *Proceedings of AIAA Aviation*, Atlanta, Georgia (AIAA, 2018).
32. M. A. Mustafa and N. J. Parziale, "Simplified read schemes for krypton tagging velocimetry in N₂ and air," *Opt. Lett.* **43**, 2909–2912 (2018).
33. A. C. Eckbreth, *Laser Diagnostics for Combustion Temperature and Species*, 2nd ed. (Gordon and Breach, 1996).
34. N. Saito, Y. Oishi, K. Miyazaki, J. Nakamura, O. Louchev, M. Iwasaki, and S. Wada, "High-efficiency generation of pulsed Lyman- α radiation by resonant laser wave mixing in low pressure Kr-Ar mixture," *Opt. Express* **24**, 7566–7574 (2016).
35. E. Clementi and C. Roetti, "Roothaan-Hartree-Fock atomic wavefunctions: basis functions and their coefficients for ground and certain excited states of neutral and ionized atoms, $z \leq 54$," *At. Data Nucl. Data Tables* **14**, 177–478 (1974).
36. A. Kramida, Y. Ralchenko, and J. Reader, and NIST ASD Team, "NIST atomic spectra database (ver. 5.5.6)," 2020, <https://physics.nist.gov/asd>.
37. H. A. Bethe and E. E. Salpeter, *Quantum Mechanics of One- and Two-Electron Atoms* (Springer-Verlag/Academic, 1957).
38. R. L. Liboff, *Introductory Quantum Mechanics*, 4th ed. (Pearson Education, 2003).
39. C. Park, *Nonequilibrium Hypersonic Aerothermodynamics*, 1st ed. (Wiley, 1990).
40. O. A. Louchev, N. Saito, K. Miyazaki, K. Okamura, J. Nakamura, M. Iwasaki, and S. Wada, "Photoionization pathways and thresholds in generation of Lyman- α radiation by resonant four-wave mixing in Kr-Ar mixture," *AIP Adv.* **6**, 1–10 (2016).
41. W. Demtröder, *Atoms, Molecules, and Photons: An Introduction to Atomic-, Molecular, and Quantum-Physics* (Springer, 2006).
42. A. Messiah, *Quantum Mechanics* (Dover Publications, 2014).
43. V. A. Kostelecký and M. M. Nieto, "Analytical wave functions for quantum-defect theory," *Phys. Rev. A* **32**, 3243–3246 (1985).
44. H. B. Bebb and A. Gold, "Multiphoton ionization of hydrogen and rare-gas atoms," *Phys. Rev.* **143**, 1–24 (1966).
45. D. A. B. Miller, *Quantum Mechanics for Engineers and Scientists* (Cambridge University, 2008).
46. M. A. Dakka, G. Tsiminis, R. D. Glover, C. Perrella, J. Moffatt, N. A. Spooner, R. T. Sang, P. S. Light, and A. N. Luiten, "Laser-based metastable krypton generation," *Phys. Rev. Lett.* **121**, 093201 (2018).